



Cite this: *Nanoscale*, 2017, **9**, 5686

Evolution of dealloying induced strain in nanoporous gold crystals†

Yu-chen Karen Chen-Wiegart,  *^{a,b} Ross Harder,^c David C. Dunand^d and Ian McNulty^e

We studied the evolution of dealloying-induced strain along the {111} in a Ag–Au nano-crystal *in situ*, during formation of nanoporous gold at the initial stage of dealloying using Bragg coherent X-ray diffractive imaging. The strain magnitude with maximum probability in the crystal doubled in 10 s of dealloying. Although formation of nano-pores just began at the surface, the greatest strain is located 60–80 nm deep within the crystal. Dealloying induced a compressive strain in this region, indicating volume shrinkage occurred during pore formation. The crystal interior showed a small tensile strain, which can be explained by tensile stresses induced by the non-dealloyed region upon the dealloyed region during volume reduction. A surface strain relaxation developed, attributed to atomic rearrangement during dealloying. This clearer understanding of the role of strain in the initial stages of formation of nanoporous gold by dealloying can be exploited for development of new sensors, battery electrodes, and materials for catalysis.

Received 14th December 2016,
Accepted 8th April 2017

DOI: 10.1039/c6nr09635b

rsc.li/nanoscale

1. Introduction

Nanoporous metals prepared by dealloying with a wide variety of metals^{1–10} have attracted great attention due to their extremely large surface-to-volume ratio which has led to numerous potential applications.^{11,12} Nanoporous gold, specifically, has been applied as an effective functional material for sensing,¹³ actuation,¹⁴ and enhanced Raman scattering,¹⁵ and used as super-capacitors,¹⁶ catalytic substrates,^{17,18} and anode substrates for Li-ion batteries.^{19,20}

Dealloying involves selectively dissolving one or more less noble element(s) from an alloy system. The atoms of the more noble element dynamically rearrange during the dealloying and form a sponge-like 3D network.²¹ It has been reported that the dealloying process may induce stress and strain which will critically impact the mechanical properties and have direct impact on the relevant applications *e.g.* surface stress-driven sensing²² and catalysis.²³

Petegem *et al.* showed that in dealloying a polycrystalline Ag–Au sample, most grains develop in-plane compressive strain and therefore are under tensile stress. The strain can be gradually released during further dealloying due to simultaneous coarsening as they reported a –0.25 to –0.07% decrease of the strain within a 4 h dealloying process.²⁴ Schofield *et al.* reported that the dealloying of Ag–Au alloy to form nanoporous gold results in two interspersed strained regions: one in significant tension and the other in compression. They interpreted this by considering regions of high positive and negative curvatures on the gold surface. The decreasing curvature, with increasing pore size, due to coarsening results in a relaxation in lattice strain.²²

However, Weissmüller pointed out that, the volume averaged pressure, which would lead to a change in the lattice parameter, is independent of the curvature. It depends solely on the volume or surface area.²⁵ The evolution of dealloying-induced strain, particularly at the early stage of dealloying, remains unexplored. Studying the initiation of the dealloying-induced strain will provide further understanding of the strain evolution. However, the X-ray methods used previously are mostly bulk, average methods; investigating the initial dealloying-induced strain, which is local and heterogeneous, requires a spatially resolved technique.

We used coherent X-ray diffractive imaging in the Bragg geometry (BCDI) in this work to quantify the dealloying-induced strain distribution in a partially dealloyed silver–gold nano-crystal, at its early dealloying stage. A unique capability of BCDI is its high sensitivity to strain in the crystal lattice. The image that is recovered from the measured diffraction patterns is typically complex, containing both magnitude and

^aDepartment of Materials Science and Chemical Engineering, Stony Brook University, Stony Brook, NY 11794, USA. E-mail: Karen.Chen-Wiegart@stonybrook.edu

^bNational Synchrotron Light Source - II, Brookhaven National Laboratory, Upton, NY 11973, USA

^cAdvanced Photon Source, Argonne National Laboratory, Argonne, IL 60439, USA

^dDepartment of Materials Science and Engineering, Northwestern University, Evanston, IL 60208, USA

^eCenter for Nanoscale Materials, Argonne National Laboratory, Argonne, IL 60439, USA

†Electronic supplementary information (ESI) available. See DOI: 10.1039/c6nr09635b

phase. The magnitude provides an image of the morphology while the phase provides an image of the displacement of the crystal lattice along the crystallographic orientation of the measured Bragg spot.^{26–29} The method has been applied to other systems where reaction induced strain play critical roles, such as cycling introduced strains in Li-ion batteries^{30,31} and hydrating phase transformation in hydrogen storage.³² In this work, we applied BCDI to study the dealloying-induced strain evolution in Ag–Au nano-crystals. We converted the measured lattice displacement into a quantitative strain distribution map as a function of position within the Ag–Au nano-crystal. These maps were produced from images of the same nano-crystal both before and after a short time of dealloying in dilute nitric acid to study the early-dealloying stage.

Nano-crystalline samples were chosen for three reasons. First, one nano-crystal contains only one or few grains. This simple system avoids the issue of having multiple grains interact with one other and therefore complicate the observed strain. Secondly, the BCDI method can be best applied to an isolated crystalline object whose size is smaller than the size of the beam. Thirdly, nano-crystals of nanoporous metals have a larger specific area compared to bulk, foil or thin film. This is critical for many applications such as sensing and actuating.

2. Results

2.1. Ag–Au nano-crystal morphological evolution with dealloying

The morphology of the as-prepared Ag–Au nano-crystals is shown in the scanning electron microscope (SEM) image in Fig. 1(a). Isolated Ag–Au crystals with sizes are 100–600 nm in diameter were made by a de-wetting fabrication process. The alloy composition of both the Ag–Au thin film and Ag–Au nano-crystals was confirmed to be identical to the Ag–30%Au target using energy-dispersive X-ray spectroscopy. Fig. 1(b) and (c) show the initial dealloying of the Ag–Au nano-

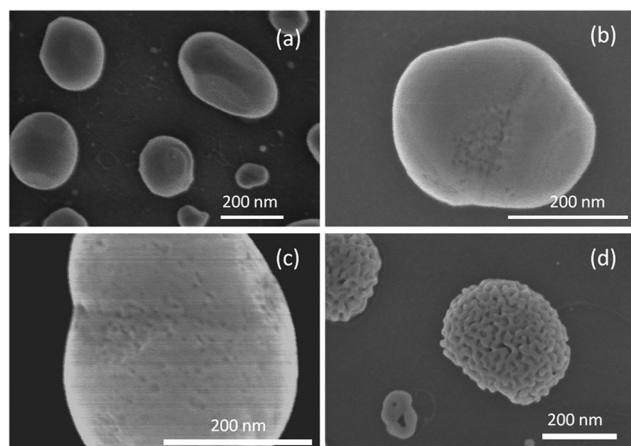


Fig. 1 SEM images of Ag–30%Au nano-crystals and formation of nanoporous Au nano-crystals (a) before dealloying, (b) 75% nitric acid, 5 s dealloying, (c) 10 s dealloying and (d) 30 s dealloying.

crystals at 5 and 10 s, respectively. Notice that the dealloying appears to start at the defects on the surface, *i.e.* the grain boundaries of the nano-crystals as seen in the 5 and 10 s of dealloying. After ~30 s of dealloying, a nanoporous Au nano-crystal was formed, as shown in Fig. 1(d).

2.2. Evolution of X-ray coherent diffraction patterns in dealloying Ag–Au nanocrystals

Fig. 2 shows a two-dimensional slice through the three-dimensional (3D) coherent diffraction patterns around the center of a Bragg spot from the same Ag–Au nano-crystal before dealloying [Fig. 2(b)] and after 10 s of dealloying to form nanoporous Au on the surface [Fig. 2(c)]. The diffraction pattern measured before dealloying was asymmetric. This indicates that some pre-existing strain was already present within the nano-crystal before dealloying. After 10 s of dealloying, speckles appeared in the coherent X-ray diffraction pattern, indicating the change in structure and strain due to dealloying. The electron density and lattice displacement of the structure can then be reconstructed from these diffraction patterns *via* a phase retrieval algorithm.

2.3. Evolution of morphology and lattice displacement in dealloying Ag–Au nano-crystals

The surfaces of the magnitude of the reconstructed complex amplitude (showing the electron density distribution) of the Ag–Au nano-crystal before and after dealloying are shown in Fig. 3(a and b). The direction of the incident X-ray beam is marked by \mathbf{k}_i , and the direction of the diffracted X-ray is

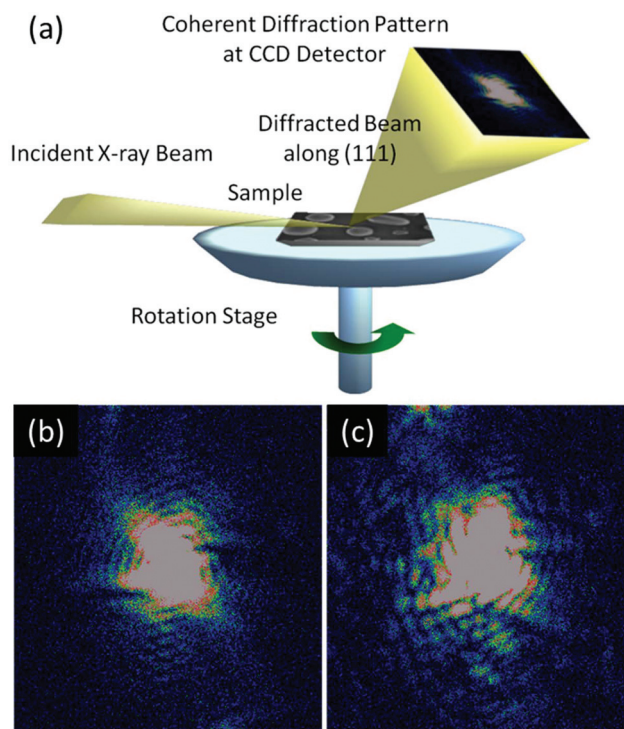


Fig. 2 (a) BCDI experimental setup. Coherent diffraction patterns around the center of a Bragg spot from a Ag–Au nano-crystal (b) before dealloying and (c) after 10 s of dealloying to form nanoporous Au on the surface.

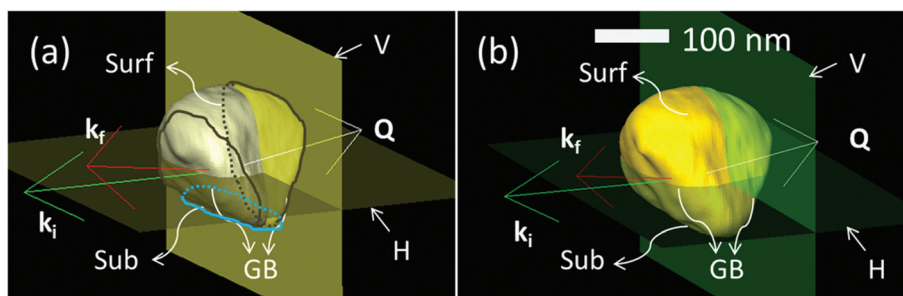


Fig. 3 Morphology of the Ag–Au nano-crystal reconstructed from BCDI patterns (a) before dealloying (b) after 10 s of dealloying. The location of the surface (Surf), substrate [Sub, indicated by blue lines in (a)] and the internal grain boundaries [GB, indicated by brown lines in (a)] are marked in the figure. The phase, displacement field and strain will be revealed at the cross-section planes – the vertical plane (V) and horizontal plane (H).

marked by \mathbf{k}_f ; \mathbf{Q} is the momentum transfer, $\mathbf{k}_f - \mathbf{k}_i$. As expected, these two images are qualitatively similar because the dealloyed Ag–Au is at a very early stage of dealloying and the initial pore size is below the resolution of the measurement.

Notice that there are two flat surfaces which are determined to be internal grain boundaries [marked as GB in Fig. 3, indicated by brown lines in Fig. 3(a)] for two reasons. Firstly, the flat shape of these two surfaces shows that these are not external surfaces, which would show a curvature as a result of dewetting [as marked “Surf” in Fig. 3(a)]. The crystal as shown in the figure therefore contains both exposed surfaces and interfaces to other grains. Secondly, this view can be supported by the analysis of the dealloying-induced strain presented at later sections. The strain evolution in the dealloyed crystal indicates that these two flat surfaces were not exposed to the nitric acid. Because the internal grain boundaries were embedded within the particle, they behave differently than the exposed surface as discussed in the later sections.

The location of the surface (Surf) and substrate [Sub, indicated by blue lines in Fig. 3(a)] are marked in the figure with the vertical (V) and horizontal (H) cross-sectional planes indicated. The phase, displacement field and strain are shown at these planes. Note that due to the twin image problem, the top and bottom of the sample cannot be determined solely from the reconstruction. However, the surface and substrate were determined based on the morphology and knowledge about the sample from the SEM images.

The short dealloying process is seen to induce a lattice displacement resulting in a phase structure in the image. Fig. 4 shows the cross-sections of the phase/lattice displacement of the Ag–Au nano-crystal. The lattice displacement in a Ag–Au crystal before dealloying [Fig. 4(a and b)] is qualitatively parallel to the surface. While during dealloying, the nano-crystal developed a much more complex internal lattice displacement structure [Fig. 4(c and d)].

The relationship between the phase (ϕ), \mathbf{k}_i , \mathbf{k}_f , \mathbf{Q} and the lattice displacement field $\mathbf{u}(x,y,z)$ can be written as:²⁸

$$\phi = \mathbf{k}_f \cdot \mathbf{u} - \mathbf{k}_i \cdot \mathbf{u} = \mathbf{Q} \cdot \mathbf{u}. \quad (1)$$

Notice that the measurement is only sensitive to the lattice displacement projected onto \mathbf{Q} , which is (111) in this work.

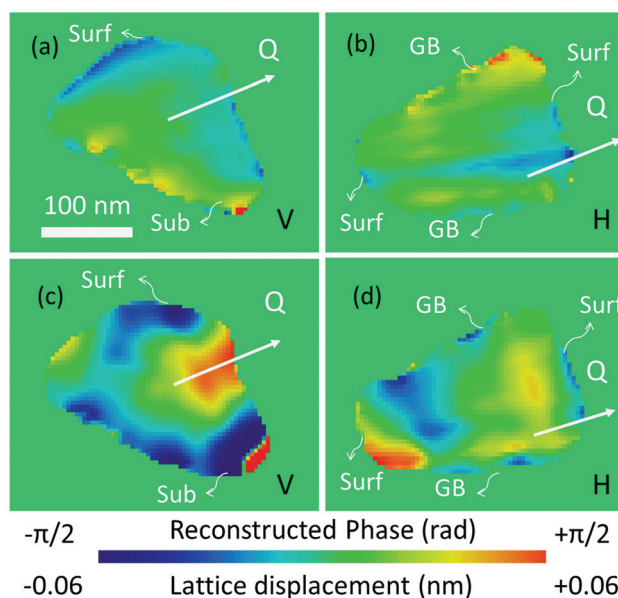


Fig. 4 The phase and lattice displacement, projected along (111), inside of the Ag–Au crystal (a–b) before dealloying [(a) vertical plane (V) marked in Fig. 3 and (b) horizontal plane (H) marked in Fig. 3]. (c–d) after 10 s of dealloying [(c) V and (d) H].

The phase (ϕ) can therefore be directly converted into the lattice displacement along (111) (u_{111}) using the following equation:

$$u_{111} = \phi / |\mathbf{Q}| = \phi / 2\pi \cdot d_{111}. \quad (2)$$

u_{111} is directly proportional to ϕ . Fig. 4 can thus also be viewed as a map of u_{111} , before and after dealloying. The \mathbf{Q} vectors marked in the figure are the projections of \mathbf{Q} onto V and H plane.

2.4. Evolution of strain in dealloying Ag–Au nano-crystals

Here, $u_{111}(x,y,z)$ is the accumulated lattice displacement relatively to the center of the crystal. The strain resulted from this lattice displacement is the change in displacement per length unit $\left(\frac{\partial l}{l}\right)$. The gradient of u_{111} , $\mathbf{\Gamma}(x,y,z)$, with respect to the lab

coordinate (x,y,z) , represents the relative distortion of the lattice caused by this lattice displacement:

$$\frac{\partial l}{l} = \Gamma(x,y,z) = \nabla u_{111} = \left(\frac{\partial u_{111}}{\partial x}, \frac{\partial u_{111}}{\partial y}, \frac{\partial u_{111}}{\partial z} \right) \quad (2)$$

Although we measured u_{111} , the lattice distortion along (111), the direction of the resulting relative distortion of the lattice is not necessarily along (111). For a location $\mathbf{r} = (x,y,z)$, $\Gamma(\mathbf{r})$ can point towards any direction, depending on the lattice distortion of the neighboring atoms.

A full strain tensor (including compressive/tensile components and shear components) can be computed if BCDI were measured for three orthogonal directions.²⁷ Here, a magnitude of the strain with contribution from mixed components was calculated to illustrate the amount of lattice distortion fraction as a result of the lattice displacement.

The relative distortion (as a result of the [111] lattice displacement) before dealloying had a maximum probability value at strain = 0.05% and mean of 0.10%. After 10 s of dealloying, the crystal developed a relative distortion of 0.10% of maximum probability, with a mean of 0.15%. The strain with maximum probability increased by factor of 2 and the mean strain increased by 50%. Note that prior to dealloying, some residual strains were observed on the surface of the crystal and also near the substrate, likely due to the geometry of the sample and the substrate constraint, respectively. These residual strain remains even after the iso-thermal heat treatment (500 °C, 6 h), part of the precursor preparation process of dewetting. These present strains and effects (from geometry and substrate) may affect the evolution of the dealloying induced-strain. Some of the significant surface strain was relieved later during dealloying. Nevertheless, the induced-strain from dealloying was observed at a deeper region, beyond the surface and substrate regions observed with high initial strain.

The greatest strain region is found near the corner of the crystal after dealloying, where the dealloying front propagated faster.³³ At 10 s of dealloying, only the Ag atoms at the surface developed pores, as shown in Fig. 1. However, the region with dealloying induced strain is as deep as 60–80 nm, as shown in the inset of Fig. 5 with circled white dotted lines. This indicates the dealloying affected the structure at this depth within 10 s. We have reported previously in dealloying a Ag–30 at%Au cylindrical sample (~16 μm in diameter), the dealloying front physically propagates at a velocity of 16 nm s⁻¹. This dealloying rate might vary due to the sample geometry.

Besides the corner of the crystal, large strain (0.2–0.5%) was also induced in the region near the substrate regions after 10 s of dealloying. A possible explanation is that, atomic rearrangement and volume shrinkage which occur during the dealloying, and due to the constraint by the substrate, a higher strain was seen at the nearby region.

To investigate the direction of the strain (tensile or compressive) induced by dealloying, we need to discuss how to convert the direction of $\Gamma(\mathbf{r})$ to the direction of the strain. The reconstructed u_{111} from the measurement is the lattice displace-

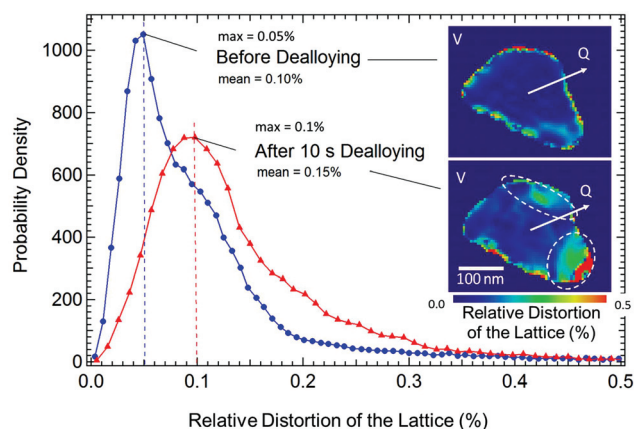


Fig. 5 Distribution of the magnitude of lattice distortion fraction induced by lattice displacement along (111). The inset shows the relative distortion of the lattice (%) distribution within of the Ag–30Au nanocrystal (from the vertical plane as shown in Fig. 3). The white dotted line indicates the region where greater strain was developed from dealloying.

ment u projected on \mathbf{Q} : $u_{111} = |\mathbf{Q}|\cos\theta$, where θ is the angle between u and \mathbf{Q} . \mathbf{Q} therefore defines the positive direction of u .

The direction of $\Gamma(\mathbf{r})$ indicates the greatest rate of increase of the lattice displacement. At a specific location \mathbf{r}_1 within the Ag–Au crystal, $\Gamma(\mathbf{r}_1)\cdot\mathbf{Q} > 0$ indicates a tensile strain because for atoms at \mathbf{r}_1 , the u_{111} of the surrounding atoms increases. On the contrary, $\Gamma(\mathbf{r}_1)\cdot\mathbf{Q} < 0$ indicates a compressive strain because for atoms at \mathbf{r}_1 , the u_{111} of the surrounding atoms decrease. An illustration of this concept can be found in ESI 2.† We can therefore determine the sign of the strain as a function of the position r within the sample, based on the sign of $\Gamma(\mathbf{r})\cdot\mathbf{Q}$.

Fig. 6 shows the probability distribution vs. strain for both dealloying and after dealloying. The general trend of the increase in both tensile and compressive strains, due to dealloying, still remains. After dealloying, the compressive strain with the maximum probability increased by factor of 1.8 and

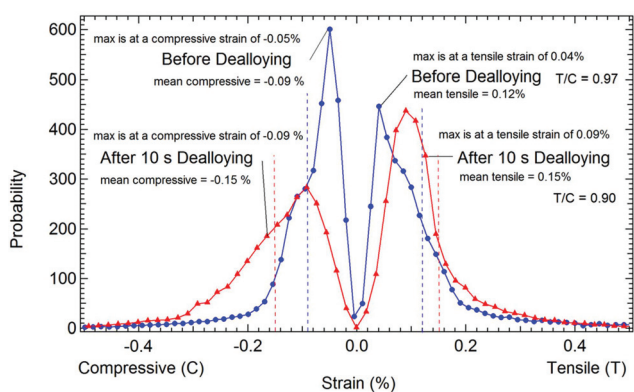


Fig. 6 Probability distribution of the compressive and tensile strain along [111], before and after dealloying. T/C is the ratio between the total probabilities of tensile strain vs. total probabilities of compressive strain.

the tensile strain with the maximum probability increased by factor of 2.25. However, the total probabilities of tensile strain vs. total probabilities of compressive strain (T/C) decreased from 0.97 to 0.90. The absolute mean compressive strain increased by 70% from -0.09% to -0.15% , while the mean tensile strain only increased by 25%, from 0.12% to 0.15% .

Fig. 7 shows the strain induced by lattice displacement along $\{111\}$ before and after dealloying within the Ag–Au crystal. The V and H planes are marked as in Fig. 3.

Before dealloying, the surface of the crystal possessed complex strain patterns mixed with tensile and compressive strains, residual from sample preparation process. The region just below the surface, up to ~ 20 nm in depth experienced slight tensile strain, likely due to surface tension, while the most part of the interior of the crystal experienced compressive strain. After 10 s dealloying, the crystal developed a region with compressive strain in the outmost region of the crystal where the dealloying occurred. Note that few boundary pixels (the outmost 2–3 pixels) may contain support errors as the values of the strain wrapping from -0.5 to 0.5 may not be physically plausible. Notice that the region next to the grain boundaries did not show the compressive strain as other surface regions, because they were embedded within the particle and were not exposed to the nitric acid; this is an evidence that these flat surfaces are indeed grain boundaries as pointed out previously. The adjacent grains would have different crystal orientations and therefore cannot be measured in the same set of Bragg peak measurement. Near the grain boundaries, a complicated strain distribution was observed, which can be attributed to the defects and mor-

phology of the grain boundaries. Significant (0.25 – 0.5%) amount of tensile strain was observed locally around both grain boundaries, along with compressive strain observed on fewer local regions. On the contrary, the interior part of the crystal shows a less amount of tensile strain after dealloying in comparison to the grain boundaries and the distribution is also more uniform. The mixed tensile and compressive surface strains were largely relaxed. High resolution transmission electron microscopy²³ showed that atomic steps and kinks are present on the surface of nanoporous gold after dealloying. While significant out-of-plane strain along $\{111\}$ was observed at the very few surface atomic layer, these surface rearrangements from dealloying may contribute to overall relaxation of the surface.

The dealloyed region shows a compressive strain, which indicates a tendency to reduce the volume during dealloying. Macroscopic volume shrinkage was reported for nanoporous gold after a complete dealloying of other Ag–Au alloy with a higher silver contents (75 – 80%).^{34,35} Although macroscopic volume shrinkage has not been reported for this alloy composition (Ag–30 at% Au), the Ag dissolution which resulted in pores within the structure may still cause instability of the Au network, leading to compressive strain. Notice that the interior part of the particle shows small tensile strain likely due to the volume reduction in dealloyed regions, which “pulled” the interior part of the crystal during its shrinkage. In some dealloyed region, tensile strain was observed. These tensile strained regions tend to be near the convex surface.

3. Conclusion

We studied the morphology and internal lattice strain of a Ag–Au nano-crystal before and after the first 10 s of nanoporous Au formation by dealloying using X-ray Bragg coherent diffractive imaging. At this initial dealloying stage, the strain with maximum probability increased by factor of two and the mean strain increased by more than 50%. The most highly strained regions occurred 60–80 nm beneath the surface, deep within the dealloyed volume. The direction of the dealloying-strain is compressive for the dealloyed region but tensile within the crystal. Our findings are consistent with Petegem *et al.*²⁴ and Schofield *et al.*²² who also observe that the dealloying induced both tensile and compressive strain at a later stage of dealloying (5 min–4 h). However, we have observed this dealloying induced strain at a much earlier stage of dealloying (10 s) and clearly identify the nanoscale spatial distribution of the strain. The compressive strain developed in the dealloyed region can be understood as the volume reduction during dealloying, which also leads to the slight tensile strain in the interior Ag–Au crystal. It cannot be observed on a macroscopic level because this increase in strain is small (0.5%), compared to the dealloying-induced strain in an alloy with higher silver content (75 or 80 at% of silver).

In summary, five types of strain evolution were observed: (1) dealloying induced a compressive strain at the dealloyed

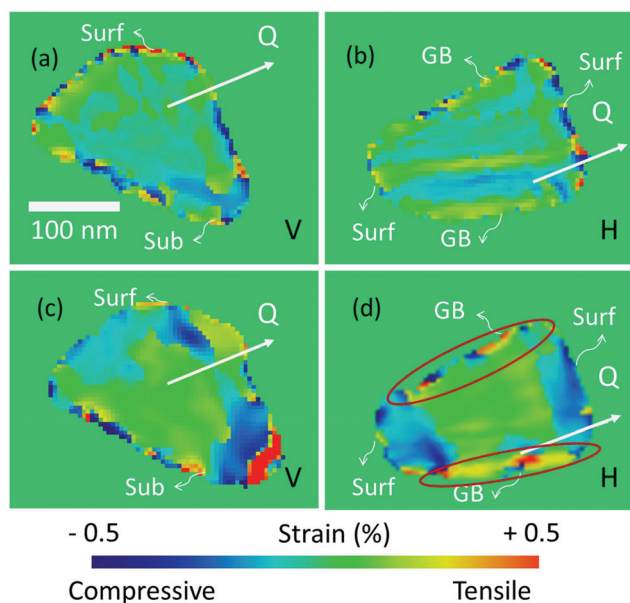


Fig. 7 Compressive and tensile strain along $\{111\}$, inside the Ag–Au crystal. Vertical and horizontal planes (a–b) before dealloying. Vertical and horizontal planes (c–d) after 10 s of dealloying. Note the strain evolved at the grain boundaries show highly local tensile strain (highlighted in dark-red circles).

region, corresponding to the volume shrinkage occurred during pore formation, (2) tensile stresses induced by the non-dealloyed region upon the dealloyed region during volume reduction, (3) a surface strain relaxation attributed to atomic rearrangement during dealloying, (4) near the substrate, the crystal atomic rearrangement was constrained and therefore a higher strain was observed, and (5) near the grain boundaries (internal interfaces embedded within the crystal) different strain evolution in the adjacent regions was observed in comparison to the free surfaces; highly local tensile and compressive strains were observed locally due to the complex defects and morphology in grain boundaries.

This clearer understanding of the role of lattice strain in the initial stages of formation of nanoporous gold by dealloying can be exploited for development of materials with novel properties. In the future, high resolution elemental mapping may be combined with strain mapping to provide further understanding in correlating the dealloying progress and the strain evolution. The ability to engineer precisely controlled strain profiles as well as porosity in nanoporous metals may find broad applications in new sensors, battery electrodes, and materials for catalysis.

4. Methods

4.1. Ag–Au nano-crystal fabrication

A thin film de-wetting method was used to fabricate the Ag–Au nano-crystals with the parameters tailored for Ag–Au alloy.²⁶ A Si wafer was cut into 5 by 5 mm² squares to serve as a substrate for the nano-crystals. Ag–30 at%Au alloy was prepared by arc melting of the pure elements (Kurt J. Lesker, 99.99%) under an argon environment. The ingot was then cold-rolled into a foil of about 200 μm thick and used as a target in the sputter deposition system. In the sputter system a plasma discharges around the target to deposit the metal onto a substrate. A 60 nm thick Ag–30%Au thin film was deposited on the Si wafer. The film was then heated to 500 °C in an argon environment for 6 hours to de-wet the film and form nano-crystals. The thin film sample was contained in a ceramic crucible covered with a lid. Silver particles (about 2–4 mm in diameter) were placed next to the sample to increase the local vapor pressure and prevent silver evaporation. The composition of the Ag–Au crystals was confirmed by energy-dispersive X-ray spectroscopy measurements, showing approximately 30–35 at % of Au. This is below the parting limit and allows dealloying process to create nanoporous structure. A dealloying test was conducted by submerging the Ag–Au crystals in 10.9 M nitric acid (75 vol% of commercial nitric acid, 68%–70% assay, in de-ionized water) for various times (5, 10, and 30 s respectively) at the room temperature (25 °C). This was done to ensure the successful formation of nanoporous gold from these nano-crystals and calibrate our acid exposure times. 10 s of dealloying time was determined to be an appropriate condition for the coherent X-ray diffraction imaging experiment.

4.2. BCDI experiment

The experimental setup is shown in Fig. 2(A). An incident X-ray beam (9 keV) was focused to approximately 1.5 μm \times 1.7 μm onto the sample at $\sim 5^\circ$. This resulted in the beam size of about 20.7 μm (perpendicular to the beam direction) by 1.7 μm (parallel to the beam direction) on the sample. A CCD detector was positioned at the (111) 2theta Bragg angle to record the coherent diffraction pattern around such a Bragg spot. The sample position was scanned until a Bragg spot from one crystal was centered on the CCD detector. By rotating the sample through $\pm 0.5^\circ$ with 0.02° in step, the full 3D coherent diffraction pattern of the sample was measured (total 51 frames). The number of slices through the 3D diffraction pattern, given by the number of angles measured, was determined such that the diffraction pattern was sampled at greater than its Nyquist frequency.³⁶ The same scan was repeated 3 times to increase the statistics.

Dealloying was performed *ex situ* by dropping nitric acid (10.9 M, 75 vol% of commercial nitric acid, 68%–70% assay, in de-ionized water; same as used in the test) directly on the sample while still in place on the diffractometer. The Ag–Au nano-crystal was dealloyed for 10 s at the room temperature and then rinsed thoroughly with de-ionized water. BCDI measurement was performed again on the partially dealloyed Ag–Au crystal. Because the sample position remained relatively untouched, the exact same crystal measured before, could be measured after being dealloying. By rotating the sample through $\pm 0.6^\circ$ with 0.02° steps, the full 3D coherent diffraction pattern of the partially dealloyed Ag–Au crystal was measured (total 61 frames). The same scan was repeated 8 times to increase the statistics. A greater number of scans was required for the dealloyed sample due to the nature of a more diffuse pattern after partial dealloying.

4.3. Data processing and phase retrieval reconstruction

The coherent X-ray diffraction data were further binned. Each of the measured BCDI patterns – before and after dealloying – was aligned by maximizing the correlation coefficient as a function of shifting one pattern relative to another. The aligned BCDI patterns were then summed.

3D complex density functions $\rho(r)$ were recovered from the summed BCDI patterns using an iterative phase retrieval algorithm.³⁶ The recovered amplitude and phase of $\rho(r)$ correspond to the electron density and lattice displacement field of the sample, respectively. The phase retrieval algorithm was applied identically to each dataset collected before and after dealloying, as described below.

A preliminary reconstruction, later used as a real-space support, was generated by reconstructing an image from the data taken before dealloying using 40 iterations of the Error Reduction algorithm (ER), then 100 iterations of the Hybrid Input Output algorithm (HIO) with a phase constraint in real space, followed by another 80 iterations of ER.³⁷ A shrink-wrap algorithm³⁷ was then applied to the reconstruction (implemented with 80 iterations of HIO then 20 iterations of ER between each update of the support), until the change in support between

cycles is less than 5%. After shrink-wrap, another 100 iterations of HIO and 80 iterations ER were performed. To use the amplitude of this preliminary reconstruction as the real-space support for further refined reconstructions, it was then thresholded to remove the low intensity noise (<1% of the maximum intensity), smoothed using 3 iterations of averaging neighboring $2 \times 2 \times 2$ voxels, and then blurred with a sigma 0.35 Gaussian blurring algorithm. This blurred amplitude was then made binary at the 1% level once again and used as a real-space support, for both data sets obtained before and after dealloying. For the final reconstruction, 40 iterations of ER, 100 iterations of HIO and then 80 iterations of ER were performed to reconstruct images in both cases. Five separate images were obtained from each data set, each time initializing the phasing algorithm with random – real numbers filling the support described earlier. The χ^2 vs. number of iterations can be found in ESI 1.† The amplitude and phase from the five reconstructed complex function were averaged separately to obtain the final images for further analysis.

The amplitude represents the electron density of the nanocrystal. A simple threshold segmentation at a value of about 10% of the maximum, was applied to the final image amplitude. A triangulated surface approximation was performed to visualize the morphology of the Ag–Au nanocrystal before and after dealloying.

The phasing algorithm might reconstruct the ‘twin’ image of the real objection because the intensity of the BCDI pattern measured at +Q is the same at –Q. A twin image is a spatially inverted object whose density is complex conjugated of the real object [$\rho \times (-r)$].³⁸ However, we can determine if the reconstructed image is the twin image by comparing the crystal shape and orientation with the SEM image for the curve surface is the surface upwards.

Acknowledgements

We are grateful to Ian Robinson for initiating the idea and helpful discussions and to Qun Shen for supporting this work through an Argonne Laboratory Directed Research and Development grant. Data collection was assisted by Xiaojing Huang and Wonsuk Cha. Xiaojing Huang also provided some of the programs used to process the data. This research used resources of the Advanced Photon Source and the Center for Nanoscale Materials, which are supported by the U.S. Department of Energy, Office of Science, Office of Basic Energy Sciences, under contract DE-AC02-06CH11357. This research used resources of the National Synchrotron Light Source II, a U.S. Department of Energy (DOE) Office of Science User Facility operated for the DOE Office of Science by Brookhaven National Laboratory under Contract no. DE-SC0012704.

References

- 1 M. E. Cox and D. C. Dunand, Bulk gold with hierarchical macro-, micro- and nano-porosity, *Mater. Sci. Eng., A*, 2011, **528**, 2401–2406.
- 2 J. Erlebacher and R. Seshadri, Hard Materials with Tunable Porosity, *MRS Bull.*, 2009, **34**, 6.
- 3 H. Q. Li, A. Misra, J. K. Baldwin and S. T. Picraux, Synthesis and characterization of nanoporous Pt–Ni alloys, *Appl. Phys. Lett.*, 2009, **95**, 201902.
- 4 X. H. Gu, L. Q. Xu, F. Tian and Y. Ding, Au–Ag Alloy Nanoporous Nanotubes, *Nano Res.*, 2009, **2**, 386–393.
- 5 M. C. Dixon, *et al.*, Preparation, structure, and optical properties of nanoporous gold thin films, *Langmuir*, 2007, **23**, 2414–2422.
- 6 L. H. Qian, W. Shen, B. Shen, G. W. W. Qin and B. Das, Nanoporous gold–alumina core–shell films with tunable optical properties, *Nanotechnology*, 2010, **21**, 7.
- 7 T. Wada, K. Yubuta, A. Inoue and H. Kato, Dealloying by metallic melt, *Mater. Lett.*, 2011, **65**, 1076–1078.
- 8 Q. Zhang, X. G. Wang, Z. Qi, Y. Wang and Z. H. Zhang, A benign route to fabricate nanoporous gold through electrochemical dealloying of Al–Au alloys in a neutral solution, *Electrochim. Acta*, 2009, **54**, 6190–6198.
- 9 Q. Chen and K. Sieradzki, Spontaneous evolution of bi-continuous nanostructures in dealloyed Li-based systems, *Nat. Mater.*, 2013, **12**, 1102–1106.
- 10 Y. C. K. Chen-wiegart, *et al.*, 3D morphological evolution of porous titanium by X-ray micro- and nano-tomography, *J. Mater. Res.*, 2013, **28**, 2444–2452.
- 11 B. C. Tappan, S. A. Steiner and E. P. Luther, Nanoporous Metal Foams, *Angew. Chem., Int. Ed.*, 2010, **49**, 4544–4565.
- 12 Y. Ding and M. Chen, Nanoporous Metals for Catalytic and Optical Applications, *MRS Bull.*, 2009, **34**, 8.
- 13 H. J. Qiu, *et al.*, Enzyme-modified nanoporous gold-based electrochemical biosensors, *Biosens. Bioelectron.*, 2009, **24**, 3014–3018.
- 14 J. Biener, *et al.*, Surface-chemistry-driven actuation in nanoporous gold, *Nat. Mater.*, 2009, **8**, 47–51.
- 15 L. H. Qian, X. Q. Yan, T. Fujita, A. Inoue and M. W. Chen, Surface enhanced Raman scattering of nanoporous gold: Smaller pore sizes stronger enhancements, *Appl. Phys. Lett.*, 2007, **90**, 3.
- 16 X. Y. Lang, A. Hirata, T. Fujita and M. W. Chen, Nanoporous metal/oxide hybrid electrodes for electrochemical supercapacitors, *Nat. Nanotechnol.*, 2011, **6**, 232–236.
- 17 A. Wittstock, V. Zielasek, J. Biener, C. M. Friend and M. Baumer, Nanoporous Gold Catalysts for Selective Gas-Phase Oxidative Coupling of Methanol at Low Temperature, *Science*, 2010, **327**, 319–322.
- 18 C. Xu, X. Xu, J. Su and Y. Ding, Research on unsupported nanoporous gold catalyst for CO oxidation, *J. Catal.*, 2007, **252**, 243–248.
- 19 Y. Yu, *et al.*, Li Storage in 3D Nanoporous Au-Supported Nanocrystalline Tin, *Adv. Mater.*, 2011, **23**, 2443–2447.
- 20 T. Wada, *et al.*, Bulk-Nanoporous-Silicon Negative Electrode with Extremely High Cyclability for Lithium-Ion Batteries Prepared Using a Top-Down Process, *Nano Lett.*, 2014, **14**, 4505–4510.

- 21 J. Erlebacher, M. J. Aziz, A. Karma, N. Dimitrov and K. Sieradzki, Evolution of nanoporosity in dealloying, *Nature*, 2001, **410**, 450–453.
- 22 E. J. Schofield, B. Ingham, A. Turnbull, M. F. Toney and M. P. Ryan, Strain development in nanoporous metallic foils formed by dealloying, *Appl. Phys. Lett.*, 2008, **92**, 3.
- 23 T. Fujita, *et al.*, Atomic origins of the high catalytic activity of nanoporous gold, *Nat. Mater.*, 2012, **11**, 775–780.
- 24 S. Van Petegem, *et al.*, On the Microstructure of Nanoporous Gold: An X-ray Diffraction Study, *Nano Lett.*, 2009, **9**, 1158–1163.
- 25 J. Weissmüller and J. W. Cahn, Mean stresses in microstructures due to interface stresses: A generalization of a capillary equation for solids, *Acta Mater.*, 1997, **45**, 1899–1906.
- 26 M. A. Pfeifer, G. J. Williams, I. A. Vartanyants, R. Harder and I. K. Robinson, Three-dimensional mapping of a deformation field inside a nanocrystal, *Nature*, 2006, **442**, 63–66.
- 27 M. C. Newton, S. J. Leake, R. Harder and I. K. Robinson, Three-dimensional imaging of strain in a single ZnO nanorod, *Nat. Mater.*, 2010, **9**, 120–124.
- 28 I. Robinson and R. Harder, Coherent X-ray diffraction imaging of strain at the nanoscale, *Nat. Mater.*, 2009, **8**, 291–298.
- 29 A. Ulvestad, *et al.*, Nanoscale strain mapping in battery nanostructures, *Appl. Phys. Lett.*, 2014, **104**, 073108.
- 30 A. Ulvestad, *et al.*, In Situ 3D Imaging of Catalysis Induced Strain in Gold Nanoparticles, *J. Phys. Chem. Lett.*, 2016, **7**, 3008–3013.
- 31 A. Ulvestad, *et al.*, Topological defect dynamics in operando battery nanoparticles, *Science*, 2015, **348**, 1344–1347.
- 32 A. Ulvestad, *et al.*, Avalanching strain dynamics during the hydriding phase transformation in individual palladium nanoparticles, *Nat. Commun.*, 2015, **6**, 8.
- 33 Y. C. K. Chen-wiegart, *et al.*, In situ imaging of dealloying during nanoporous gold formation by transmission X-ray microscopy, *Acta Mater.*, 2013, **61**, 1118–1125.
- 34 Y. C. K. Chen-wiegart, S. Wang, I. McNulty and D. C. Dunand, Effect of Ag-Au composition and acid concentration on dealloying front velocity and cracking during nanoporous gold formation, *Acta Mater.*, 2013, **61**, 5561–5570.
- 35 S. Parida, *et al.*, Volume change during the formation of nanoporous gold by dealloying, *Phys. Rev. Lett.*, 2006, **97**, 035504.
- 36 R. Harder, M. A. Pfeifer, G. J. Williams, I. A. Vartanyants and I. K. Robinson, Orientation variation of surface strain, *Phys. Rev. B: Condens. Matter*, 2007, **76**, 115425.
- 37 R. Harder, M. Liang, Y. Sun, Y. Xia and I. K. Robinson, Imaging of complex density in silver nanocubes by coherent X-ray diffraction, *New J. Phys.*, 2010, **12**, 035019.
- 38 M. Watari, *et al.*, Differential stress induced by thiol adsorption on faceted nanocrystals, *Nat. Mater.*, 2011, **10**, 862–866.